

www.acsnano.org

Interfacial Electromechanics Predicts Phase Behavior of 2D Hybrid Halide Perovskites

Christopher C. Price, Jean-Christophe Blancon, Aditya D. Mohite, and Vivek B. Shenoy*



Cite This: ACS Nano 2020, 14, 3353-3364



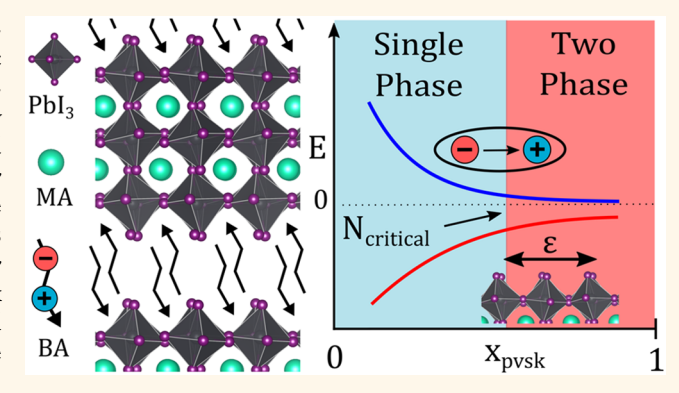
ACCESS

Metrics & More

Article Recommendations

SI Supporting Information

ABSTRACT: Quasi-two-dimensional (2D) mixed-cation hybrid halide perovskites ($A'_2A_{N-1}M_nX_{3N+1}$; A' = large organic molecule with cationic group, $A = [Cs^+, CH_3NH_3^+, HC-(NH_2)_2^+]$, M = [Pb, Sn, Ge], $X = [I^-, Br^-, Cl^-]$) have rapidly emerged as candidates to improve the structural stability and device lifetime of 3D perovskite semiconductor devices under operating conditions. The addition of the large A' cation to the traditional AMX_3 structure introduces several synthetic degrees of freedom and breaks M-X bonds, giving rise to peculiar critical phase behavior in the phase space of these complex materials. In this work, we propose a thermodynamic model parametrized by first-principles calculations to generate the phase diagram of 2D and quasi-2D perovskites (q-2DPKs)



based on the mechanics and electrostatics of the interface between the A' cations and the metal halide octahedral network. Focusing on the most commonly studied methylammonium lead iodide system where A' is n-butylammonium (BA; $CH_3(CH_2)_3NH_3^+$), we find that the apparent difficulty in synthesizing phase-pure samples with a stoichiometric index N > 5 can be attributed to the energetic competition between repulsion of opposing interfacial dipole layers and mechanical relaxation induced by interfacial stress. Our model shows quantitative agreement with experimental observations of the maximum phase-pure stoichiometric index (N_{crit}) and explains the nonmonotonic evolution of the lattice parameters with increasing stoichiometric index (N). This model is generalizable to the entire family of q-2DPKs and can guide the design of photovoltaic and optical materials that combine the structural stability of the q-2DPKs while retaining the charge carrier properties of their 3D counterparts.

KEYWORDS: 2D hybrid organic—inorganic perovskite, interfacial dipole, multiscale modeling, critical phase behavior, surface stress

ybrid organic-inorganic lead halide perovskites $(AMX_3; A = small organic or large alkali cation, M$ = Pb, Sn, Ge, X = I, Br, Cl) have been extensively studied as ideal solution-processable semiconductors with excellent visible-range optical properties, but they have been crippled by their thermodynamic instability to water erosion in ambient conditions. 1-5 Replacing a portion of the A cations with hydrophobic large organic molecules (A') can lead to layered perovskite structures where the intercalated large molecules interrupt the MX3 octahedral network, resulting in a self-assembled organic-inorganic lamellar composite material that resists moisture degradation. 6-10 Synthetic advances such as hot-casting have led to increased control over the growth orientation and stoichiometric ratio of these $A'_2A_{N-1}M_NX_{3N+1}$ compounds (A' = large organic molecule), where the stoichiometric index N corresponds to the ratio of hydrophobic cations to perovskite semiconductor. 8,11-16 In singlephase materials, manipulation of the chemical composition (N) controls the thickness of the perovskite layer and thus the

magnitude of quantum and dielectric confinement effects on the electronic and optical properties. This makes these materials an ideal optoelectronics platform even beyond their enhanced stability. ²⁴

The compositional phase space of these materials is vast due to the chemical degrees of freedom at each site in the structure, particularly at the organic A and A' sites. Most studies have focused on the A' = n-butylammonium (BA; $CH_3(CH_2)_3NH_3^+$), A = methylammonium (MA; $CH_3NH_3^+$), M = Pb, X = I system; this was one of the first 2D perovskites synthesized, and its 3D analogue MAPbI3 is the most widely studied member of the 3D hybrid perovskites. In pure phases, this material has been frequently reported and studied in the

Received: November 17, 2019 Accepted: February 19, 2020 Published: February 19, 2020



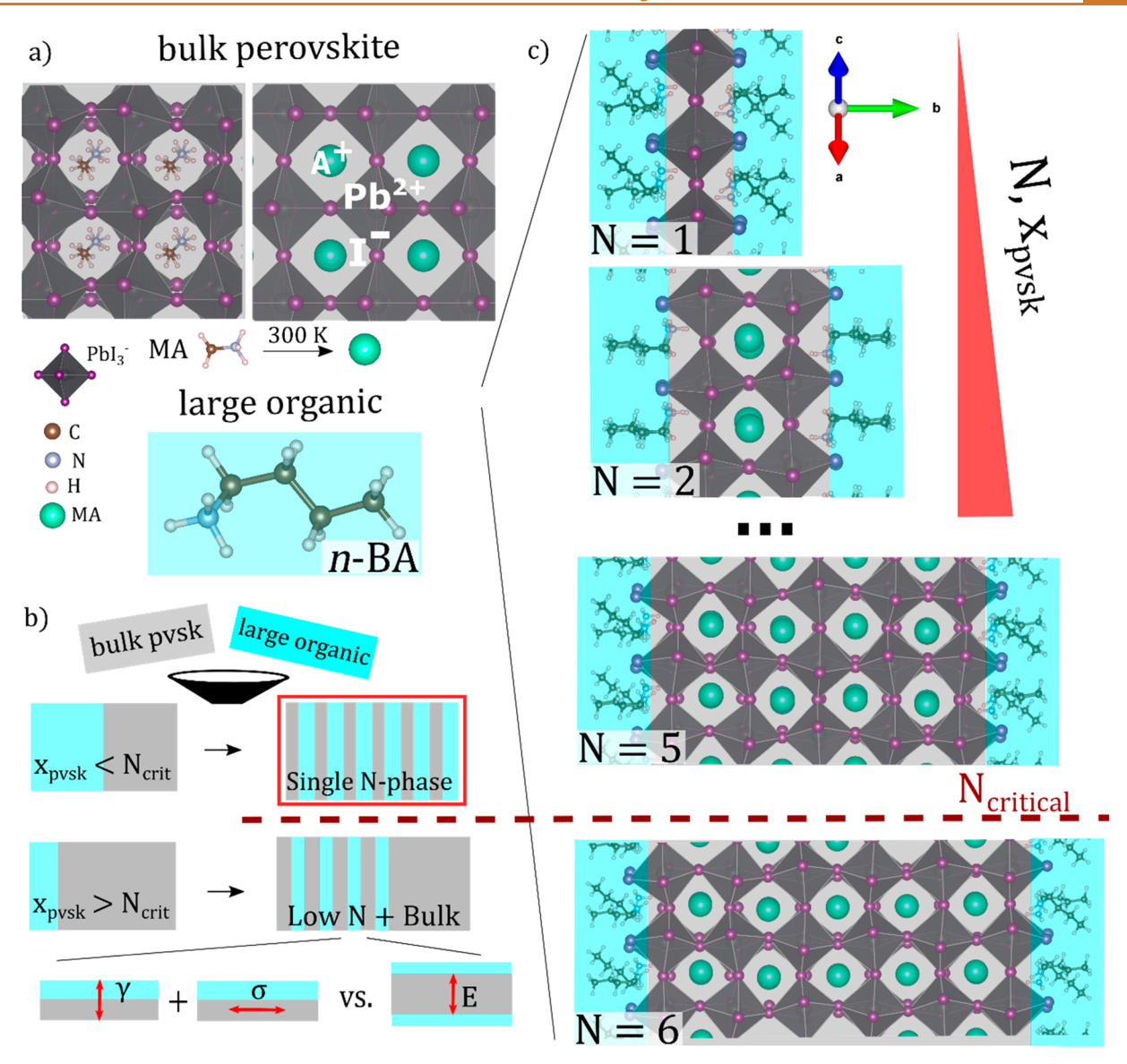


Figure 1. (a) Atomistic overview of the parent perovskite phase (MAPbI₃) in low- and room-temperature structures; replacing some MA with an A' cation (n-butylammonium) leads to the layered structures in (b). (b) Quasi-unit cells of the 2D layered perovskites. N counts the number of PbI₃ octahedra between large organic layers; phases with N > 5 (N_{crit}) are not synthesized in phase-pure form. (c) Macroscopic thermodynamic outcomes of the two-component A' (cyan) + bulk (gray) perovskite composite material. For uniform electronic properties, a single N-phase (red box) morphology is ideal.

low-N phases $(N < 5)^{6,8,12,13,16,25-32}$ and reported only twice for $N > 5.^{33,34}$ In these recent studies, Soe *et al.* found it more difficult to isolate single crystals of the higher N phases, finding impurity phases in the XRD spectra at stoichiometric ratios corresponding to N = 6, 7, and 9 with the amount of multiphase mixing increasing with N. Mao *et al.* reported similar results for their Ruddlesden-Popper N = 7 synthesis and suggested that the growth environment is kinetically constrained. Recently expanding synthetic efforts have focused primarily on varying the A' cation; examples include guanidinium (GA), 35 phenylethylammonium (PEA), $^{36-39}$ fluoro-PEA (f-PEA), 40 N, N-dimethylphenylene-p-diammonium (DPDA), 41 n-propylammonium (PA), 42 n-pentylammonium (PA), 43 n-hexylammonium (PA), 43 and (A)-(aminomethyl) piperidinium (A)-(A)

synthesized with an average stoichiometry $\langle N \rangle$ = (10, 20, 40, 60) phases consisting of a mix of competing phases, and 4-AMP has been synthesized in the N=7 pure phase. 15,34

The gap in the single-phase behavior at the critical N value of 5 for BA and other linear-chain A' cations is surprising since both the low N < 5 and very high $N = \infty$ (bulk) phases are readily synthesized. Single-phase intermediate N compounds would improve carrier transport by reducing exciton binding energies while retaining the highly ordered layered structure and creating opportunities for favorable band alignment in heterostructures. However, it is difficult to draw general physical insights about this phase behavior from the synthetic efforts discussed above due to the multitude of thermodynamic and kinetic factors varying between studies. In this work, we develop a continuum thermodynamic model parametrized by atomistic first-principles density functional theory (DFT) calculations to map the phase space and study the critical phase behavior of the quasi-2D layered perovskites (q-2DPKs).

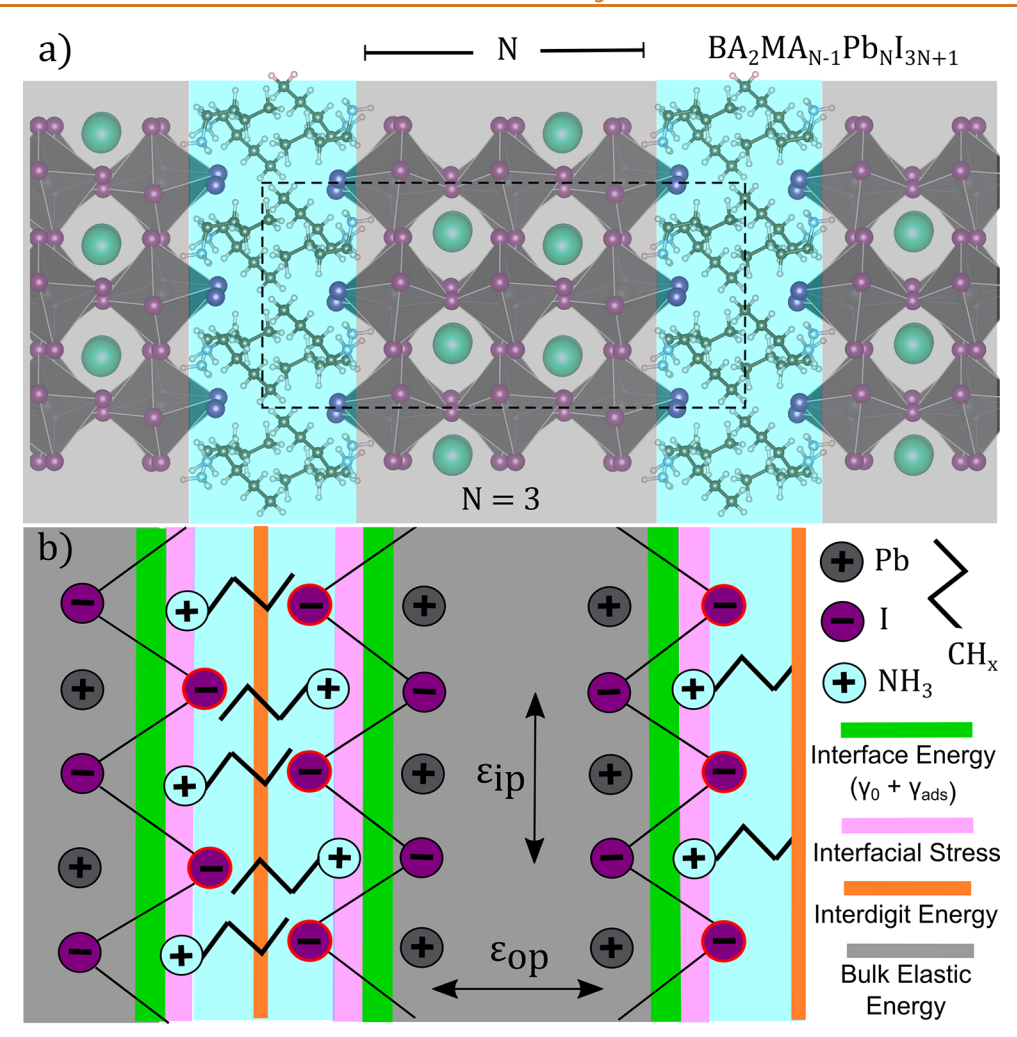


Figure 2. (a) Zoomed view of the periodic layered perovskite structure. The dashed line shows the slab unit cell used to parametrize the continuum model. (b) Schematic for the basis of the continuum model. The interfaces are denoted by the undercoordinated iodine atoms (red outline) where the BA cation has broken the Pb–I bond. The key interactions are shown in green (interfacial energy: surface energy + adsorption energy), pink (interfacial stress of the perovskite), orange (interdigitation energy of the BA molecules), and gray (perovskite layer with bulk elastic energy). The elastic degrees of freedom are the in-plane strain $\varepsilon_{\rm ip}$ and out-of-plane strain $\varepsilon_{\rm op}$.

Focusing on the A' = BA system as a representative example, we find that the critical N value of 5 arises from electromechanical competition between the interfacial stress of the MX₃ octahedral network and the interfacial dipole interactions across the inorganic layer. We show that this competition also drives nonmonotonic evolution of the lattice parameters with N, which is relevant to the electronic properties of each phase. We find that the N critical value can be tuned through the interfacial dipole moment, which can be constructed as a sum of the surface dipole moment of the bulk perovskite and the intrinsic dipole moment of the A' cation. This means that the choice of A' cation can have an equal or greater impact on the structural phase space than the choice of the specific perovskite network. These results will enable engineering of phase-pure q-2DPKs in intermediate composition ranges with long-term thermodynamic stability for enhanced electronic and optical properties.

RESULTS

Atomistic Overview and Model Approach. We first map the family of q-2DPK to a two-component mixture of A' cations and bulk 3D perovskite (PK) that forms a composite

system of layers (Figure 1a,c), focusing on the system where A' = BA and PK = MAPbI₃. At 300 K, MAPbI₃ forms in a tetragonal phase with nearly isotropic rotational disorder of the MA cations. 45 The Pb2+ and MA+ cations are caged in an electron-accepting iodine network, which forms corner-sharing octahedra around the lead ions. To replicate this, we fix the lattice parameters in the tetragonal configuration and use green spheres to represent the MA+ cations; the orientation of the MA cations has been shown to negligibly impact the electronic properties. 11,46 Further details can be found in the Methods and Supporting Information. The BA A' cation is composed of a four-carbon backbone with an NH₃⁺ ammonium group at one end. When substituted for MA in the bulk perovskite, the long carbon chains interrupt the halide network, leading to alternating layers of A' cation (BA2)2+ and perovskite $(A_{N-1}Pb_NI_{3N+1})^{2-}$ with a thickness corresponding to the A/ A' stoichiometric ratio. The quasi-unit cells of these structures are shown in Figure 1c. The full unit cell includes two A' cation layers and two perovskite layers due to the Ruddlesden-Popper stacking, with experimentally characterized space groups of C2cb for odd-N phases and Cc2m for even-N phases. 6,33,47 With such a large number of atoms in the unit cell for N > 1 structures, it is practically impossible to

perform wide-ranging *ab initio* calculations on the family of q-2DPKs, and the few existing modeling reports are based on semiempirical approaches. This greatly emphasizes the need for a continuum model to describe the thermodynamics of these materials. The layered structures undergo a small (<2%) orthorhombic distortion from the tetragonal MAPbI₃ parent phase at 300 K, which we ignore in the model for simplicity. 11

The stoichiometric index N corresponds to the amount of BA cation incorporated into the structure and can be visualized as the number of PbI₃ octahedra spanning the inorganic layer in the b lattice direction. We also define the perovskite atom fraction x_{pvsk} as the fraction of atoms in the sample that do not belong to the BA cation. Figure 1b outlines how x_{pvsk} , N, and the critical N value (N_{crit}) are related; for a composition x_{pvsk} of bulk perovskite and BA cations corresponding to a single phase N value $\leq N_{\text{crit}}$ single-phase crystals are observed. For x_{pvsk} compositions corresponding to $N > N_{crit}$, two-phase or multiphase mixtures of low-N $(N < N_{crit})$ phases and bulk perovskite $(N = \infty)$ are observed. The homogeneous morphologies highlighted in red are desirable for well-defined optical and electronic properties. Recent results have indicated that N_{crit} is dependent on the A' cation chosen in the system,³⁴ and different choices of A and A' cations may prevent layered composite formation altogether. In our model, we propose that $N_{\rm crit}$ is not a spurious kinetic effect but emerges as a result of thermodynamic competition between the mechanics of the composite interface and the electrostatic repulsion of adjacent interfaces across the perovskite layer.

Strain-Dependent Free Energy of the Composite A'/
Perovskite System. To develop general insights about the composite layered organic—inorganic system, we map the atomistic structure into a continuum model of interacting slabs with two BA-adsorbed interfaces, as shown by the black dashed box in Figure 2a. As in Figure 1, we color-code the "bulk" perovskite regions gray and the all-organic BA regions cyan and identify the critical chemical and mechanical variables contributing to the thermodynamics of the mixture. The overall chemical reaction forming the layered structure is

$$2BAI_{(s)} + PbI_{2(s)} + (N-1)MAPbI_{3(s)}$$

$$\rightarrow BA_{2}MA_{N-1}Pb_{N}I_{3N+1(s)}$$
(1)

We begin by writing the total free energy of the system as $G_{\text{tot}} = G_0 + \Delta G_{\text{mix}}$, where $G_0 = x_{\text{BAI}}G_0^{\text{BAI}} + x_{\text{MAPbI}_3}G_0^{\text{MAPbI}_3} + x_{\text{PbI}_2}G_0^{\text{PbI}_2}$ gives the composition-weighted free energy of formation of the q-2DPK components and ΔG_{mix} captures the free energy of mixing the constituents. $G_0^{\text{Pbl}_2}$ is necessary to describe the N=1compound where the A' cation has replaced all of the A cation, but since this is the lower limit of the stoichiometric range we are interested in, it can be added into $G_0^{\mathrm{MAPbI_3}}$ as a constant, which is done from here on. Since the layered phases are all highly ordered and the entropy of crystallization for BAI is small,⁴⁸ we take $S_0 \approx 0$ and $\Delta S_{\text{mix}} \approx 0$. With these simplifications, we can use the composition fraction $x_{
m pvsk}$ introduced earlier $G_0 = (1 - x_{\text{pvsk}})H_0^{\text{BAI}} + x_{\text{pvsk}}H_0^{\text{MAPbI}_3}$ and $\Delta G_{\text{mix}} = \Delta H_{\text{mix}}$. As an atom fraction, $x_{\text{pvsk}} = \frac{n_{\text{pvsk}}}{n_{\text{tot}}}$, where n_{pvsk} is the number of atoms belonging to the perovskite layer and n_{tot} is the total number of atoms in one formula unit of $BA_2MA_{N-1}Pb_NI_{3N+1}$.

Based on the atom counts in each component, x_{pvsk} and N are related through $N = \frac{27 + 7x_{\text{pvsk}}}{12(1 - x_{\text{pvsk}})}$. The formation energies of the bulk components are calculated from atomic reference states using DFT according to the following reactions:

$$H_0^{\text{BAI}} = \Delta H_f: 4C_{(s)} + \frac{1}{2}N_2 + \frac{1}{2}I_2 + 6H_2$$

$$\to CH_3(CH_2)_3NH_3I \tag{2}$$

 $H_0^{\mathrm{MAPbI}_3}$

$$= \Delta H_{f}: \begin{cases} Pb_{(s)} + I_{2} \rightarrow PbI_{2} & N = 1\\ 2Pb_{(s)} + \frac{5}{2}I_{2} + \frac{1}{2}N_{2} + C_{(s)} + 3H_{2} & N > 1\\ \rightarrow MAPbI_{3} + PbI_{2} & (3) \end{cases}$$

where $MA = CH_3NH_3$.

Next, we develop the mixing enthalpy ΔH_{mix} of the BA cations and bulk perovskite, which describes the 2D interfaces formed on each side of the perovskite slab (Figure 2b). The interfacial energy (green) is a combination of the energy cost of cleaving the perovskite by breaking the Pb-I bonds γ_0 and the adsorption energy γ_{ads} of the large organic cations onto the cleaved perovskite surface. The sum of γ_0 and γ_{ads} gives the mechanically uncoupled interfacial energy; these and other material parameters described below are calculated using DFT, as detailed in the Methods and Supporting Information (Table S3). Based on experimental evidence, ^{6,33} the lattice parameters of the layered structure evolve with N, so we introduce two elastic degrees of freedom within the gray perovskite domain only: the in-plane strain parallel to the interface $\varepsilon_{\rm ip}$ and the outof-plane strain perpendicular to the interface $\varepsilon_{\mathrm{op}}$, which are taken relative to the PK experimental lattice constants at room temperature measured by Whitfield et al.45 These strain degrees of freedom contribute through the interfacial stress $f_{\rm ss}=\frac{\partial \gamma_0}{\partial \varepsilon_{\rm ip}}\varepsilon_{\rm ip}$ (Figure 2b, pink) and the bulk elastic energy for a tetragonal $E_{\rm B} = \frac{1}{2} (2C_{11}\varepsilon_{\rm ip}^2 + C_{22}\varepsilon_{\rm op}^2 + 4C_{12}\varepsilon_{\rm op}\varepsilon_{\rm ip} + 2C_{13}\varepsilon_{\rm ip}^2), \text{ where } C_{ij}$ are the elastic stiffness constants in Voigt notation. These two terms compete due to the different bonding environments at the organic-inorganic interface and the interior of the perovskite slab. f_{ss} is parametrized by calculating the linear change of the free perovskite surface energy γ_0 with in-plane strain ε_{ip} (Figure S2), while E_B is calculated using the elastic constants of bulk MAPbI₃.^{51,52} The corresponding elastic energy of the soft organic layer and organic contributions to f_{ss} are verified to be small in comparison and ignored, but the van der Waals (vdW) interactions between the BA molecules belonging to adjacent interfaces are captured by $U_{\rm interdigit}$ (Figure 2b, orange). This is calculated as the energetic difference between isolated symmetric BA-adsorbed perovskite slabs (Figure S1c) and the fully periodic layered structure (Figure S1d). Normalized to energy per atom, the straindependent energy of forming the individual A'/perovskite interfaces is

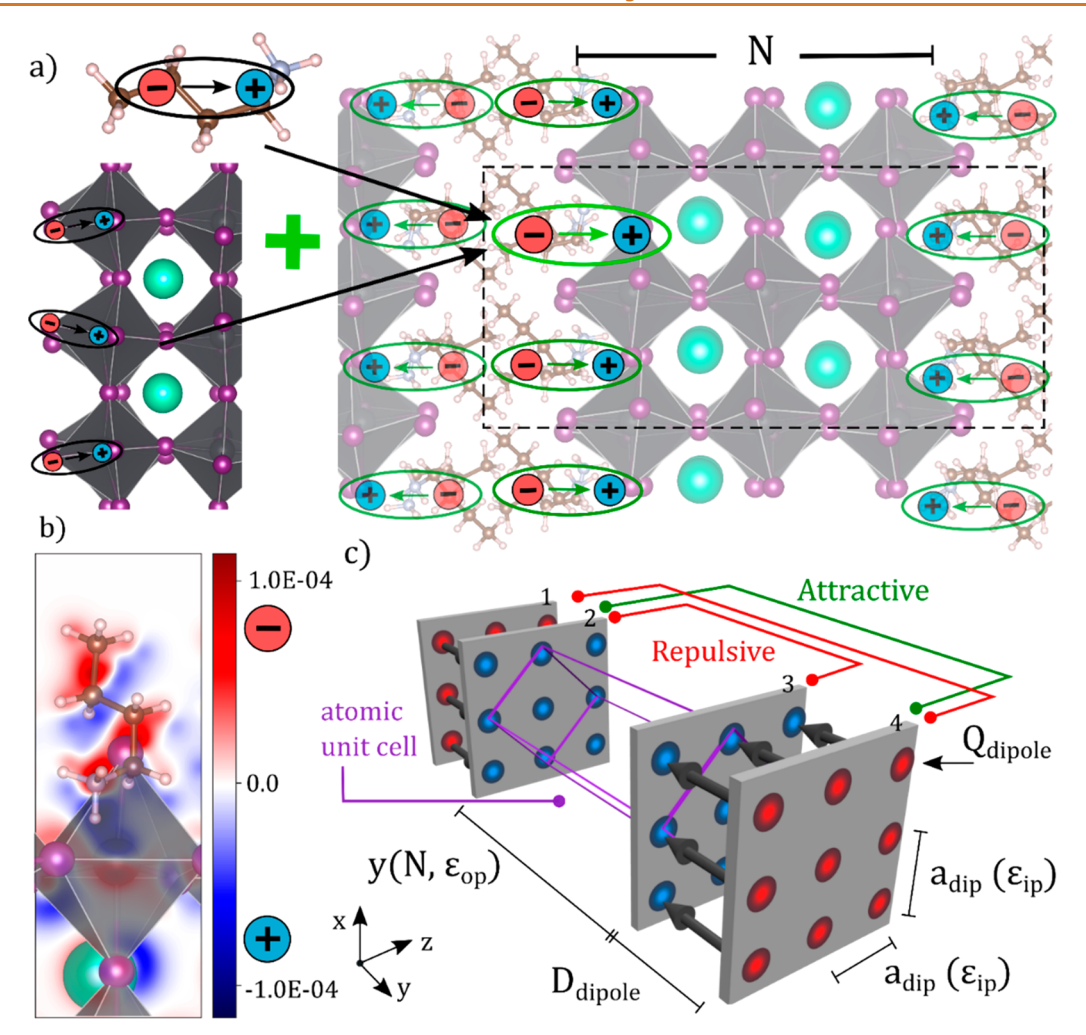


Figure 3. (a) Atomistic schematic for the formation and alignment of interfacial dipoles. The dipole moment of the BA cation aligns with the I-terminated surface dipole of the perovskite surface (left), which we sum to an effective interfacial dipole (green) perpendicular to the interface. (b) Bonding electronic charge density of the BA-perovskite adsorbed surface projected along the (001) direction showing significant out-of-plane polarization; units in e/\dot{A}^3 . (c) Schematic of the dipole lattice model and the N-dependent electrostatic interaction. The cross-interface distance and the dipole planar lattice constant are coupled to $\varepsilon_{\rm op}$ and $\varepsilon_{\rm ip}$, respectively.

$$E_{\text{interface}} = \frac{A_0}{n_{\text{tot}}} \left(\gamma_0 + \gamma_{\text{ads}} + U_{\text{interdigit}} + \frac{\partial \gamma_0}{\partial \varepsilon_{\text{ip}}} \varepsilon_{\text{ip}} \right) + V_0 x_{\text{pvsk}} E_{\text{B}}(\varepsilon_{\text{ip}}, \varepsilon_{\text{op}})$$
(4)

where A_0 is the unstrained surface area, V_0 is the unstrained volume of the bulk perovskite unit cell, and $n_{\rm tot}$ is the total number of atoms in one composite formula unit. After parametrization by DFT calculations (details in SI), we find that the interface formation governed by the above expression is thermodynamically favorable ($E_{\rm interface} < 0$) at all reasonable strains and compositions due to the strongly negative $\gamma_{\rm ads}$. This is not surprising since the low-N layered compounds with high interfacial area are readily synthesized, but it does not explain the critical N behavior.

Electrostatic Interactions of Adjacent Interfacial Dipole Layers. Since we are interested in the relative energies between phases with varying perovskite thickness N, this picture of the enthalpy of mixing is incomplete. Along with the overall composition and frequency of interfaces, the main structural feature that varies with N is the distance between two interfaces across the perovskite layer. The formation of

surface dipole layers has been studied extensively in ionic perovskites, but less so in hybrid halide perovskites due to the mixed ionic/covalent nature of the bonds and variable stoichiometry at free surfaces. 53-56 Due to the broken Pb-I bonds and the change in the organic cation at the interface, interfacial dipole layers can form and provide a mechanism for the interfaces to interact electrostatically across the perovskite slab. Figure 3a gives a schematic view of how the combination of the NH₃⁺ cation and the undercoordinated I atoms at the organic-inorganic interface can be mapped to a 2D lattice of effective interfacial dipoles with the in-plane periodicity of the BA cations. Figure 3b shows the bonding charge density, defined as the difference between the electronic density of the interface and the isolated neutral component atoms, projected along the (001) direction. Red regions indicating localization of electronic density (negative charge) and blue regions indicating absence of electron density relative to isolated neutral atoms provide a first-principles justification of the outof-plane polarization localized around the BA molecule. We focus on the interfacial interaction across the perovskite layer since this distance is N-dependent; while adjacent interfaces are closer together across the organic layer, this interaction length is essentially invariant with N. Furthermore, this

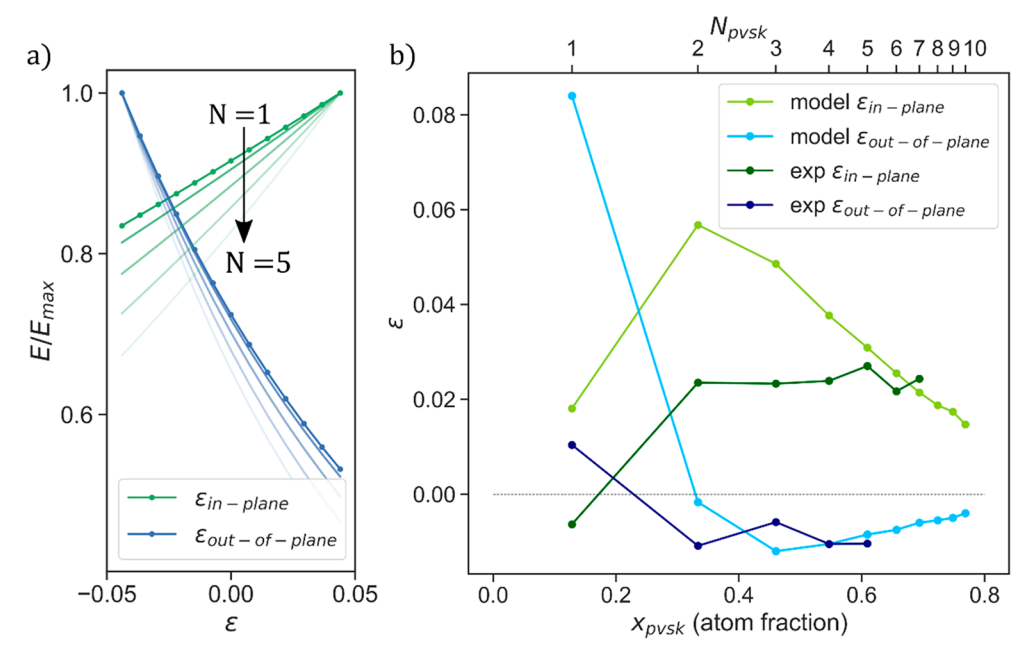


Figure 4. (a) Strain dependence of the electrostatic dipole energy as a function of N, normalized in terms of the max dipole energy value over the strain window. A 10% strain window corresponds to a \sim 20% energy change at N=1 and a \sim 35% change at N=5. (b) Experimental versus model strain as a function of N. The model qualitatively captures the nonmonotonic behavior of the strain and the switch from N=1 to 2 from out-of-plane positive (in-plane negative) to out-of-plane negative (in-plane positive) strain.

interfacial interaction across the organic layer is already incorporated into the vdW interaction energy $U_{\rm interdigit}$ discussed above.

While the electric potential between equally and uniformly charged sheets is zero by superposition, inhomogeneities in the charge density due to the ionic nature of the BA cation groups and the I⁻ atoms lead to corrugations in the potential and a finite contribution to the electrostatic energy. To capture the point charge lattice physics, we construct two opposing dipole arrays consisting of 2D square lattices of charged Gaussian disks (Figure 3c) and map the relevant parameters $(N, \, \varepsilon_{\rm ip}, \, \varepsilon_{\rm op})$ from the A' cation/perovskite mixture model in Figure 2. We also introduce two parameters, $Q_{\rm dipole}$ and $D_{\rm dipole}$, which represent the magnitude and distance of the charge separation for each dipole in the lattice; the dipole moment is equal to $Q_{\rm dipole}*D_{\rm dipole}$. The electrostatic energy $U_{\rm E}$ of a stack of 2D point charge lattices with equal periodicity and overall charge neutrality is given by

$$U_{\rm E} = \frac{A}{2\varepsilon_r} \sum_{k_{xz\neq 0}} \sum_{i < j} \frac{\widetilde{\sigma_i}(k_x, k_z)^* \widetilde{\sigma_j}(k_x, k_z)}{|\vec{k}|} \exp(-|y_i - y_j||\vec{k}|)$$
(5)

where the area of each 2D unit cell A and the in-plane reciprocal lattice vectors \vec{k} depend on $\varepsilon_{\rm ip}$ and the perpendicular distance between sheets $|y_i-y_j|$ depends on $\varepsilon_{\rm op}$ (relationship shown in Figure 3c; parameter values and details of the derivation in the SI). $\varepsilon_{\rm r}$ is the static permittivity of the medium, 21,59 $\tilde{\sigma}$ are the Fourier coefficients of the real-space charge distribution, and i,j are the integer indexes of the sheets in the stack (Figure S4). The static dielectric constant $\varepsilon_{\rm r}$ in MAPbI₃ is difficult to measure or calculate but depends on the presence of surfaces and the slab thickness; for simplicity, we choose a global average value of 12 between N=1 and bulk and ignore any thickness (y) dependence. Especially, for the

three interactions we consider between the dipole sheets $i, j \in \{1, 2, 3, 4\}$:

$$\begin{aligned} |y_1 - y_3| &= Nb_0(1 + \varepsilon_{\text{op}}) + D_{\text{dipole}} \\ |y_2 - y_3| &= Nb_0(1 + \varepsilon_{\text{op}}) \\ |y_1 - y_4| &= Nb_0(1 + \varepsilon_{\text{op}}) + 2D_{\text{dipole}} \end{aligned}$$

where b_0 is the unstrained lattice constant of the bulk perovskite perpendicular to the (010) surface. Equation 5 shows that the electrostatic energy decays exponentially with the distance between the charge sheets with a characteristic length that depends on the in-plane lattice constant through the reciprocal vector k. The asymptotic behavior interpolates between the limiting cases of uniformly charged sheets ($U_{\rm E}$ = 0) and a single dipole-dipole interaction at long-range ($U_{\rm E} \approx$ $1/r^3$), consistent with the construction of an infinite series of screened dipole—dipole interactions. The appearance of $\varepsilon_{\rm ip}$ and $\varepsilon_{
m op}$ in the exponential couples the energy of electrostatic interfacial interactions with the energy of mechanical interface relaxation described in Figure 2b. The relative strain dependence of the electrostatic energy is shown in Figure 4a over several different reference $|y_i - y_j|$ corresponding to different *N*-phases from N = 1 to N = 5. A crucial point that emerges is that the direction of the strain dependence opposes that of the interfacial stress relaxation f_{ss} ; while the electrostatic cross-interface interaction energy $U_{\rm E}$ is minimized with compressive in-plane strain and tensile out-of-plane strain, the individual interfacial energy $E_{\rm interface}$ is lowered through tensile in-plane strain and an elastically induced compressive out-of-plane strain.

Minimization of the Free Energy and Determination of N_{crit} . The value and strain dependence of the electrostatic term suggests that it will compete with the interfacial mechanical relaxation, but quantifying this competition requires minimizing the free energy. Combining all the

energetic contributions to the formation of 2D perovskites listed above, we can write down the complete expression for $\Delta H_{\rm mix}$ and the total free energy (using the atom fraction conversion $N=\frac{27+7x_{\rm pvsk}}{12(1-x_{\rm must})}$):

$$G_{\text{tot}}(x_{\text{pvsk}}, \, \varepsilon_{\text{ip}}, \, \varepsilon_{\text{op}})$$

$$= x_{\text{pvsk}} H_0^{\text{MAPbI}_3} + (1 - x_{\text{pvsk}}) H_0^{\text{BAI}}$$

$$+ \Delta H_{\text{mix}}(x_{\text{pvsk}}, \, \varepsilon_{\text{ip}}, \, \varepsilon_{\text{op}})$$
(6)

$$\Delta H_{\text{mix}} = \frac{A_0}{n_{\text{tot}}} \left(\gamma_0 + \gamma_{\text{ads}} + U_{\text{interdigit}} + \frac{\partial \gamma_0}{\partial \varepsilon_{\text{ip}}} \varepsilon_{\text{ip}} \right) + V_0 x_{\text{pvsk}} E_{\text{B}}(\varepsilon_{\text{ip}}, \varepsilon_{\text{op}}) + \frac{U_{\text{E}}(\varepsilon_{\text{ip}}, \varepsilon_{\text{op}}, N)}{n_{\text{tot}}}$$
(7)

At each composition $x_{\text{pvsl}\nu}$ G_{tot} can be minimized with respect to the internal degrees of freedom ε_{ip} and ε_{op} to find the minimum free energy at each composition $G_{\min}(N)$ and construct the phase diagram. Due to the discrete sums in U_{E} , we minimize this expression numerically, but we note that the primary scaling of the free energy at the minimum strain occurs with composition, as each term of ΔH_{\min} in eq 7 scales as $\frac{1}{N}$,

 x_{pvsk} and $\frac{\exp(-N)}{N}$, respectively. In Figure 4b, we use the strain values which minimize the free energy at each composition to compare the equilibrium structures predicted by our model with experimental lattice constants measured at room temperature. 6,7,33,60 Both the experimental and model strains are calculated as deviations from the bulk tetragonal MAPbI₃ structure determined by Whitfield et al. 45 We find that the model semiquantitatively captures the nonmonotonic trend of the lattice parameters from N = 1 to N = 5. The in-plane strain is determined as the change in area of the (010) plane of the layered structure from the equivalent (101) plane in the bulk reference structure. At N = 1, the interfacial electrostatic interaction dominates the single-interface mechanics, and the perovskite lattice experiences in-plane compression and out-ofplane tension. Increasing to N = 2 reverses this effect, and the increased distance between the interfaces allows the interfacial mechanics to dictate the structure. The disagreement in the magnitude of the structural distortion for the N = 1 phase stems from an increase of the elastic moduli of the perovskite layer (nanoscale hardening) at N = 1 and a breakdown of the continuum approximation that the single octahedral layer of the N = 1 structure can be accurately modeled by two independent interfaces. This raises the point that while the leading order contributions of the interface elastic energy are captured by $\frac{\partial \gamma_0}{\partial e_{\rm ip}}$, a higher order strain term of the form $\frac{1}{2}AE_8e^2$

could also be included, where A is the area, $E_{\rm S}$ are the surface elastic constants, and ε is the strain tensor. This term is second order in strain and therefore small relative to the energy differences between ordered phases at small N; we have dropped this term from the model to simplify the parameter space. Despite this, the dielectric approximation, and the tetragonal symmetry approximation, the salient features of the structural evolution are captured. This has important effects on the trends of band gap evolution in these materials. 62

Having benchmarked the mechanical results of the model with experiment, we now plot the minimum free energy curve as a function of composition to examine the thermodynamic

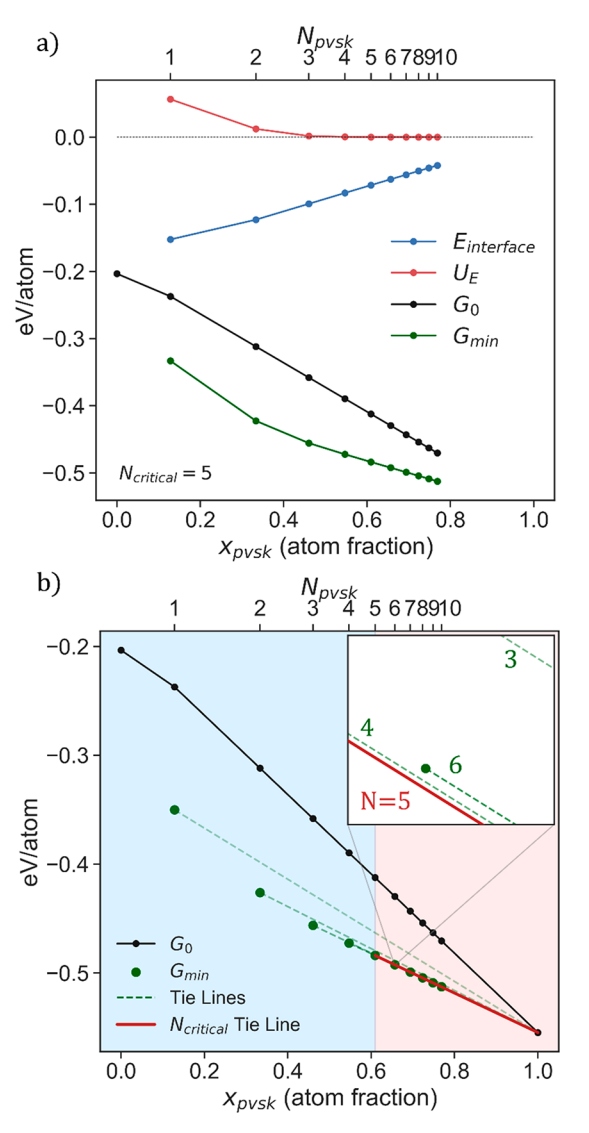


Figure 5. (a) Component curves for the free energy minimized with respect to strain. The independent bulk formation energy G_0 (black), interfacial energy $E_{\rm interface}$ (blue), and electrostatic energy $U_{\rm E}$ (red) combined to give the minimized energy of the ordered phases $G_{\rm min}$ (green). (b) Determination of $N_{\rm crit}$ using tie lines with the bulk formation energy. Blue region indicates compositions where single ordered phases (green dots) are stable with respect to phase mixing; red region indicates compositions where two-phase separation is thermodynamically preferred.

competition between ordered phases at different compositions. Figure 5a shows how the different components of G_{\min} (green) scale with composition x_{pvsk} and N, up to N = 10. Immediately, we see that the repulsive electrostatic energy (red) between the interfaces competes with the energetically favorable surface relaxation (blue) of low-N structures. The nature of this competition is determined by the magnitude of the surface energy and interfacial stress, the elasticity of the octahedral network, and the magnitude of the interfacial dipoles. At low-N compositions, the proximity of the interfaces increases the energy of the system, while at high-N compositions, the electrostatic interaction decays to zero and the reduction of the interfacial energy through mechanical relaxation takes over. Without the electrostatic terms, the two-phase mixture of highly strained thin (N = 1) phase and nonstrained excess bulk $(N = \infty)$ is preferred at all compositions (Figure S3) since this

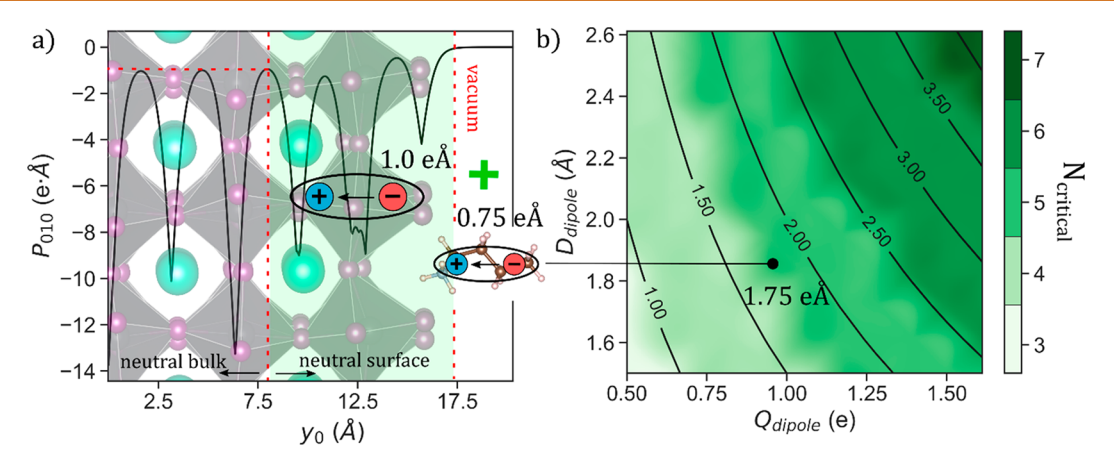


Figure 6. (a) Determination of the surface dipole moment of MAPbI₃ and BA. The local maxima in the dipole moment indicates that the symmetric slab is divided into charge-neutral portions, leading to a physically meaningful dipole value. We take the converged value from the interior of the slab. (b) $N_{\rm crit}$ (green) mapped over the interfacial dipole lattice parameters $Q_{\rm dipole}$ and $D_{\rm dipole}$, with all other parameters held equal. The sum of the surface moment and cation moment fall in the $N_{\rm crit}$ = 5 range for BA₂MA_{N-1}Pb_NI_{3N+1}. The $N_{\rm crit}$ changes follow the isomoment Q*D contours in black, and sensitive changes in the moment induce changes in the $N_{\rm crit}$ value.

two-phase configuration maximizes the number of thermodynamically favorable interfaces while reducing the total bulk elastic energy of the perovskite. The electrostatic repulsion of the interfaces incurs an energy penalty at low N and leads to an inflection point in G_{\min} that corresponds to N_{crit} . The strain coupling of these competing mechanisms is necessary to accurately locate this inflection point, which is quite sensitive to the relative magnitudes of the two effects. In Figure 5b, we zoom in on the total energy curve (green) to extract N_{crit} which is the ordered phase nearest the inflection point of ΔH_{\min} . Specifically, the N_{crit} point is the minimum N composition corresponding to an ordered N phase which is not thermodynamically stable with respect to a two-phase mixture satisfying the composition constraint:

$$\begin{split} G_{\min}(N_{\text{crit}}+1) &> X_1 G_{\min}(N < N_{\text{crit}}) \\ &+ X_2 G_{\min}(N > N_{\text{crit}}); \ x_{\text{tot}} = x_{\text{pvsk}}^{N_{\text{crit}}} \end{split} \tag{8}$$

where X_1 and X_2 are phase fractions that satisfy the total composition constraint x_{tot} . Graphically, this is visualized by drawing tie lines between different phases on the minimum free energy composition curve; the highest single-phase composition that is not superseded by a tie line between other phases corresponds to $N_{\rm crit}$. This superseding tie line is drawn in red and originates at N = 5 in Figure 5b, indicating that the model predicts an N_{crit} of 5 in $BA_2MA_{N-1}Pb_NI_{3N+1}$, in agreement with general experimental observations (Table S2). While the energy differences are small between the different ordered phases on a per-atom basis, over several formula units the thermodynamic driving force becomes significant. The shallow curvature of G_{\min} in the region of the inflection point means that the N = 4 and N = 6 phases are close in energy over a range of compositions. This is supported by the synthesis trend in the literature, as observing N = 5 and N > 5 phases is less frequent and less phase-pure over N = 4 compounds (Table S2). This indicates that kinetic freedom (such as hotcasting) during synthesis also plays a significant role in differentiating these compounds.⁶⁰

Interfacial Dipoles Enable Synthetic Control of $N_{\rm crit}$. The energetic competition between interface formation and cross-interface interaction can lead to critical phase behavior, but we seek to develop a deeper connection between the

schematic dipole lattice in Figure 3, which is constructed of equal and opposite point charges and parametrized by Q_{dipole} and $D_{
m dipole}$, and the continuous charge distribution of the atomistic interface. Dipole moments of continuous charge distributions are only well-defined in the presence of a finite surface. 63 The dipole moment of a charge distribution perpendicular to a (010) surface can be calculated as $P_{010} = \int_{y_0}^{b_0} (y - y_0) \rho(y - y_0) dy$, where y_0 is a coordinate reference point inside the charge distribution and b_0 is the length of the supercell perpendicular to the surface. 64 Figure 6a plots this surface dipole value as a function of the reference point y_0 for the bulk perovskite surface that corresponds crystallographically to the interface that forms in the q-2DPK compounds. The local maxima correspond to the points where v_0 divides $\rho(v)$ into two charge-neutral halves, so that the dipole value at these reference points is both physically meaningful and far enough from the surface that it is converged. From this analysis, we find that the surface dipole moment for the perovskite is 1.0 eÅ. Since the BA cation is an overall neutral single molecule with a finite charge distribution in all dimensions, the dipole moment can be easily found by $P = \int \vec{r} \cdot \rho(\vec{r}) d\vec{r}$, which we calculate to be 0.75 eÅ.

The wide array of possible A' cationic molecules indicates that an ideal strategy to tune the phase behavior of the q-2DPK is through the induced interfacial dipole moment as opposed to the perovskite elasticity. Figure 6b shows the evolution of $N_{
m crit}$ as a function of the electrostatic lattice parameters $Q_{
m dipole}$ and D_{dipole} (Figure 3c), with the iso-moment contours $\hat{P} =$ $Q_{\text{dipole}}*\hat{D}_{\text{dipole}}$ shown in black. All other model parameters, such as the interfacial energy and interfacial stress, are held constant. First, we find that $N_{\rm crit}$ evolves along the iso-moment contours over independent variations of Q_{dipole} and D_{dipole} , which presents a qualitative affirmation that the dipolar interactions can modify the critical phase behavior. Second, we note that by taking the interfacial dipole moment as a sum of the perovskite surface dipole and the dipole moment of an isolated n-BA cation, we match the dipole moment of ~1.75 eÅ required in the model to observe $N_{\rm crit}$ = 5. This simple relation allows for prediction of the N_{crit} value based on the properties of the individual A' cation molecules, which is otherwise difficult to calculate using first-principles calculations due to the numerous degrees of freedom and the difficulty of describing long-range electrostatic interactions using pseudopotential DFT. The ability to obtain the interfacial dipole as a sum of the independent components can be attributed to the hydrogenic bonding between the organic cations and the lead halide network; if the A' molecule forms covalent bonds with the iodine-rich perovskite surface and significant charge transfer occurs at the interface, this simple design rule may not hold. However, since the interfacial dipole moment is notoriously difficult to calculate or measure directly, this decomposition into readily calculable dipole moments has significant predictive power.

The sensitivity of the $N_{\rm crit}$ value to the interfacial dipole moment shows that tuning the interfacial composition can have a substantial impact on the thermodynamically accessible synthesis space of quasi-2D hybrid perovskites. Recently, successful synthesis of an N=7 q-2DPK with greater phase purity than BA was achieved using 4-AMP (Table S1) as the A' cation, an organic molecule with two different cationic groups on each end.³⁴ Returning to the derivation of $U_{\rm E}$, we note that the nonlattice average charge density contributions to the interior electric field from each interface caused a cancellation in the contributions of the electric field scaling as $\frac{1}{y_0}$ with interfacial separation. As characterized, the 4-AMP

compound aligns with its neighbors to maximize conjugate ring interactions, breaking the symmetry between the perovskite interfaces and introducing another contribution to the interior electric field. Since our model predicts that increasing the electrostatic energy will shift the critical point to higher N_1 these molecules with asymmetric cationic groups are highly promising for tunably expanding the q-2DPK into the quasibulk, nonexcitonic regime. Altering the small A cation may also enable engineering of the critical phase boundary. For example, formamidinium (FA) in place of MA increases the lattice constant of the lead iodide octahedra, 65 increasing the dipole lattice spacing and the internal electrostatic energy. Competing changes may occur to other parameters such as the dielectric constant, so a complete parameter study using our model is warranted to predict the outcome of these chemical substitutions.

CONCLUSIONS

Surveying the synthetic efforts in the fast-growing field of 2D and quasi-2D organic-inorganic halide perovskites, we set out to identify the governing thermodynamic mechanisms of the compositional phase space by considering the free energy of formation of the composite structures. We found that thermodynamically favorable adsorption of large organic molecules onto the I-terminated perovskite surface and interfacial mechanical relaxation drive the formation of internal interfaces to maximize the interfacial area while minimizing the elastic energy penalty. This effect competes with the unfavorable electrostatic interaction between the two opposing perovskite interfacial dipole lattices associated with the adsorbed large organic molecules. The interfacial mechanical relaxation and the electrostatic energy are coupled through the in-plane and out-of-plane strain, which is found to evolve nonmonotonically from low-N to high-N phases matching experimental trends. Together, these effects lead to a finite N_{crit} which corresponds to the minimum loading of A' cations in the $A'_2A_{N-1}M_NX_{3N+1}$ compositional formula to obtain thermodynamically stable single phases. At $N > N_{crit}$, the

system will preferentially phase separate into a mixture of bulk perovskite $(N=\infty)$ and $N \leq N_{\rm crit}$. We find that $N_{\rm crit}$ can be tuned by reasonable modifications of the interfacial dipole value and that this complicated quantity can be sufficiently approximated by the sum of the perovskite surface dipole and the dipole moment of the isolated A' cation. Our multiscale, first-principles informed continuum model provides a mechanistic understanding and synthetic guidance in the large compositional phase space of quasi-2D perovskites.

METHODS

DFT Calculations. First-principles DFT simulations were carried out using the Vienna ab initio simulation package (VASP).66 Projector-augmented wave pseudopotentials⁶⁸ are used with a cutoff energy of 520 eV for plane-wave expansions.⁶⁹ The exchangecorrelation is treated using the Perdew-Burke-Ernzerhof (PBE) generalized gradient approximations. The atomistic structures of isolated, symmetric perovskite slabs were relaxed using Γ -centered kpoint meshes of $7 \times 1 \times 7$, while fully periodic structures were sampled at $7 \times 3 \times 7$. Bulk structures are relaxed using similar meshes of $7 \times 5 \times 7$. For structural relaxations, the atomic positions of all unit and supercells are optimized until the force components on each atom are less than 0.005 eV/Å, and the electronic energy is converged within 10⁻⁸ eV. Tight convergence criteria are required due to the shallow nature of the perovskite potential energy surface. A vacuum spacing of 20 Å was added to slab calculations to prevent interactions between periodic images, as well as dipole corrections to the energy and potential in the case of isolated molecules or asymmetric slabs. Long-range van der Waals dispersion interactions between organic and inorganic components were treated using the DFT-D3 method developed by Grimme et al. 70,71 Following previous studies, 11 the lattice parameters were fixed in a tetragonal configuration for atomic relaxations to simulate the room-temperature phase of MAPbI₃, and Cs atoms were used instead of MA cations to increase the rotational symmetry of the A cation site and reduce computational cost (Figure S1a, S1b). All calculated properties were verified to be minimally affected by the cation switch.

ASSOCIATED CONTENT

Supporting Information

The Supporting Information is available free of charge at https://pubs.acs.org/doi/10.1021/acsnano.9b09105.

Chemical formulas and depictions of experimentally used A' cations; survey of experimental syntheses of *n*-BA q-2DPKs; relevant model parameters and their descriptions; representative atomistic supercells used in DFT calculations; calculation of surface stress energy; phase diagram calculated without electrostatic energy contributions; methods discussion for bulk, interfacial, and elastic energy contributions; derivation of electrostatic energy of interfacial dipole arrays (PDF)

AUTHOR INFORMATION

Corresponding Author

Vivek B. Shenoy — Department of Materials Science and Engineering, University of Pennsylvania, Philadelphia, Pennsylvania 19104, United States; Email: vshenoy@seas.upenn.edu

Authors

Christopher C. Price – Department of Materials Science and Engineering, University of Pennsylvania, Philadelphia, Pennsylvania 19104, United States; orcid.org/0000-0002-4702-5817

Jean-Christophe Blancon – Department of Chemical and Biomolecular Engineering, Rice University, Houston, Texas 77005, United States

Aditya D. Mohite — Department of Chemical and Biomolecular Engineering, Rice University, Houston, Texas 77005, United States; orcid.org/0000-0001-8865-409X

Complete contact information is available at: https://pubs.acs.org/10.1021/acsnano.9b09105

Notes

The authors declare no competing financial interest.

ACKNOWLEDGMENTS

This work is supported primarily by contract W911NF-16-1-0447 from the Army Research Office (V.B.S.) and also by grants EFMA-542879 and CMMI-1727717 from the U.S. National Science Foundation. A.D.M. acknowledges funding from DOE-EERE 2022-1652.

REFERENCES

- (1) Ono, L. K.; Juarez-Perez, E. J.; Qi, Y. Progress on Perovskite Materials and Solar Cells with Mixed Cations and Halide Anions. ACS Appl. Mater. Interfaces 2017, 9, 30197–30246.
- (2) Qiu, L.; Ono, L. K.; Qi, Y. Advances and Challenges to the Commercialization of Organic–Inorganic Halide Perovskite Solar Cell Technology. *Mater. Today Energy* **2018**, *7*, 169–189.
- (3) Fu, Q.; Tang, X.; Huang, B.; Hu, T.; Tan, L.; Chen, L.; Chen, Y. Recent Progress on the Long-Term Stability of Perovskite Solar Cells. *Adv. Sci.* **2018**, *5*, 1700387.
- (4) Yang, J.; Siempelkamp, B. D.; Liu, D.; Kelly, T. L. Investigation of CH₃NH₃PbI₃ Degradation Rates and Mechanisms in Controlled Humidity Environments Using In Situ Techniques. *ACS Nano* **2015**, 9. 1955–1963.
- (5) Frost, J. M.; Butler, K. T.; Brivio, F.; Hendon, C. H.; van Schilfgaarde, M.; Walsh, A. Atomistic Origins of High-Performance in Hybrid Halide Perovskite Solar Cells. *Nano Lett.* **2014**, *14*, 2584–2590.
- (6) Stoumpos, C. C.; Cao, D. H.; Clark, D. J.; Young, J.; Rondinelli, J. M.; Jang, J. I.; Hupp, J. T.; Kanatzidis, M. G. Ruddlesden–Popper Hybrid Lead Iodide Perovskite 2D Homologous Semiconductors. *Chem. Mater.* **2016**, *28*, 2852–2867.
- (7) Mitzi, D. B. Synthesis, Crystal Structure, and Optical and Thermal Properties of $(C_4H_9NH_3)_2MI_4$ (M = Ge, Sn, Pb). *Chem. Mater.* **1996**, *8*, 791–800.
- (8) Tsai, H.; Nie, W.; Blancon, J.-C.; Stoumpos, C. C.; Asadpour, R.; Harutyunyan, B.; Neukirch, A. J.; Verduzco, R.; Crochet, J. J.; Tretiak, S.; Pedesseau, L.; Even, J.; Alam, M. A.; Gupta, G.; Lou, J.; Ajayan, P. M.; Bedzyk, M. J.; Kanatzidis, M. G.; Mohite, A. D. High-Efficiency Two-Dimensional Ruddlesden—Popper Perovskite Solar Cells. *Nature* **2016**, *536*, 312–316.
- (9) Calabrese, J.; Jones, N. L.; Harlow, R. L.; Herron, N.; Thron, D. L.; Wang, Y. Preparation and Characterization of Layered Lead Halide Compounds. *J. Am. Chem. Soc.* **1991**, *113*, 2328–2330.
- (10) Smith, I. C.; Hoke, E. T.; Solis-Ibarra, D.; McGehee, M. D.; Karunadasa, H. I. A Layered Hybrid Perovskite Solar-Cell Absorber with Enhanced Moisture Stability. *Angew. Chem., Int. Ed.* **2014**, 53, 11232—11235
- (11) Kepenekian, M. L.; Traore, B.; Blancon, J.-C.; Pedesseau, L.; Tsai, H.; Nie, W.; Stoumpos, C. C.; Kanatzidis, M. G.; Even, J.; Mohite, A. D.; Tretiak, S.; Katan, C. Concept of Lattice Mismatch and Emergence of Surface States in Two-Dimensional Hybrid Perovskite Quantum Wells. *Nano Lett.* **2018**, *18*, 5603–5609.
- (12) Chen, A. Z.; Shiu, M.; Ma, J. H.; Alpert, M. R.; Zhang, D.; Foley, B. J.; Smilgies, D.-M.; Lee, S.-H.; Choi, J. J. Origin of Vertical Orientation in Two-Dimensional Metal Halide Perovskites and Its Effect on Photovoltaic Performance. *Nat. Commun.* **2018**, *9*, 1336.
- (13) Zhang, X.; Munir, R.; Xu, Z.; Liu, Y.; Tsai, H.; Nie, W.; Li, J.; Niu, T.; Smilgies, D.-M.; Kanatzidis, M. G.; Mohite, A. D.; Zhao, K.; Amassian, A.; Liu, S. Phase Transition Control for High Performance

- Ruddlesden-Popper Perovskite Solar Cells. Adv. Mater. 2018, 10, 1707166.
- (14) Hu, J.; Oswald, I. W. H.; Stuard, S. J.; Nahid, M. M.; Zhou, N.; Williams, O. F.; Guo, Z.; Yan, L.; Hu, H.; Chen, Z.; Xiao, X.; Lin, Y.; Yang, Z.; Huang, J.; Moran, A. M.; Ade, H.; Neilson, J. R.; You, W. Synthetic Control over Orientational Degeneracy of Spacer Cations Enhances Solar Cell Efficiency in Two-Dimensional Perovskites. *Nat. Commun.* **2019**, *10*, 1276.
- (15) Quintero-Bermudez, R.; Gold-Parker, A.; Proppe, A. H.; Munir, R.; Yang, Z.; Kelley, S. O.; Amassian, A.; Toney, M. F.; Sargent, E. H. Compositional and Orientational Control in Metal Halide Perovskites of Reduced Dimensionality. *Nat. Mater.* **2018**, *17*, 900–907.
- (16) He, X.; Wang, Y.; Li, K.; Wang, X.; Liu, P.; Yang, Y.; Liao, Q.; Zhai, T.; Yao, J.; Fu, H. Oriented Growth of Ultrathin Single Crystals of 2D Ruddlesden—Popper Hybrid Lead Iodide Perovskites for High-Performance Photodetectors. ACS Appl. Mater. Interfaces 2019, 11, 15905—15912.
- (17) Papavassiliou, G. C.; Koutselas, I. B. Structural, Optical and Related Properties of Some Natural Three- and Lower-Dimensional Semiconductor Systems. *Synth. Met.* **1995**, *71*, 1713–1714.
- (18) Tanaka, K.; Kondo, T. Bandgap and Exciton Binding Energies in Lead-Iodide-Based Natural Quantum-Well Crystals. *Sci. Technol. Adv. Mater.* **2003**, *4*, 599–604.
- (19) Katan, C.; Mercier, N.; Even, J. Quantum and Dielectric Confinement Effects in Lower-Dimensional Hybrid Perovskite Semiconductors. *Chem. Rev.* **2019**, *119*, 3140–3192.
- (20) Ishihara, T.; Takahashi, J.; Goto, T. Optical Properties Due to Electronic Transitions in Two-Dimensional Semiconductors-(C_nH_{2n+1}NH₃)₂PbI₄. *Phys. Rev. B: Condens. Matter Mater. Phys.* **1990**, 42, 11099–11107.
- (21) Traore, B.; Pedesseau, L.; Assam, L.; Che, X.; Blancon, J.-C.; Tsai, H.; Nie, W.; Stoumpos, C. C.; Kanatzidis, M. G.; Tretiak, S.; Mohite, A. D.; Even, J.; Kepenekian, M. L.; Katan, C. Composite Nature of Layered Hybrid Perovskites: Assessment on Quantum and Dielectric Confinements and Band Alignment. *ACS Nano* **2018**, *12*, 3321–3332.
- (22) Blancon, J.-C.; Stier, A. V.; Tsai, H.; Nie, W.; Stoumpos, C. C.; Traoré, B.; Pedesseau, L.; Kepenekian, M.; Katsutani, F.; Noe, G. T.; Kono, J.; Tretiak, S.; Crooker, S. A.; Katan, C.; Kanatzidis, M. G.; Crochet, J. J.; Even, J.; Mohite, A. D. Scaling Law for Excitons in 2D Perovskite Quantum Wells. *Nat. Commun.* **2018**, *9*, 2254.
- (23) Even, J.; Pedesseau, L.; Katan, C. Understanding Quantum Confinement of Charge Carriers in Layered 2D Hybrid Perovskites. *ChemPhysChem* **2014**, *15*, 3733–3741.
- (24) Pedesseau, L.; Sapori, D.; Traore, B.; Robles, R.; Fang, H.-H.; Loi, M. A.; Tsai, H.; Nie, W.; Blancon, J.-C.; Neukirch, A.; Tretiak, S.; Mohite, A. D.; Katan, C.; Even, J.; Kepenekian, M. Advances and Promises of Layered Halide Hybrid Perovskite Semiconductors. *ACS Nano* **2016**, *10*, 9776–9786.
- (25) Gélvez-Rueda, M. C.; Hutter, E. M.; Cao, D. H.; Renaud, N.; Stoumpos, C. C.; Hupp, J. T.; Savenije, T. J.; Kanatzidis, M. G.; Grozema, F. C. Interconversion between Free Charges and Bound Excitons in 2D Hybrid Lead Halide Perovskites. *J. Phys. Chem. C* 2017, 121, 26566–26574.
- (26) Silver, S.; Yin, J.; Li, H.; Brédas, J.-L.; Kahn, A. Characterization of the Valence and Conduction Band Levels of *n* = 1 2D Perovskites: A Combined Experimental and Theoretical Investigation. *Adv. Energy Mater.* **2018**, *8*, 1703468.
- (27) Liu, J.; Leng, J.; Wu, K.; Zhang, J.; Jin, S. Observation of Internal Photoinduced Electron and Hole Separation in Hybrid Two-Dimentional Perovskite Films. *J. Am. Chem. Soc.* **2017**, *139*, 1432–1435.
- (28) Tu, Q.; Spanopoulos, I.; Yasaei, P.; Stoumpos, C. C.; Kanatzidis, M. G.; Shekhawat, G. S.; Dravid, V. P. Stretching and Breaking of Ultrathin 2D Hybrid Organic–Inorganic Perovskites. *ACS Nano* **2018**, *12*, 10347–10354.
- (29) Raghavan, C. M.; Chen, T.-P.; Li, S.-S.; Chen, W.-L.; Lo, C.-Y.; Liao, Y.-M.; Haider, G.; Lin, C.-C.; Chen, C.-C.; Sankar, R.; Chang, Y.-M.; Chou, F.-C.; Chen, C.-W. Low-Threshold Lasing from 2D

- Homologous Organic-Inorganic Hybrid Ruddlesden-Popper Perovskite Single Crystals. *Nano Lett.* **2018**, *18*, 3221–3228.
- (30) Lin, Y.; Bai, Y.; Fang, Y.; Chen, Z.; Yang, S.; Zheng, X.; Tang, S.; Liu, Y.; Zhao, J.; Huang, J. Enhanced Thermal Stability in Perovskite Solar Cells by Assembling 2D/3D Stacking Structures. *J. Phys. Chem. Lett.* **2018**, *9*, 654–658.
- (31) Leng, K.; Abdelwahab, I.; Verzhbitskiy, I.; Telychko, M.; Chu, L.; Fu, W.; Chi, X.; Guo, N.; Chen, Z.; Chen, Z.; Zhang, C.; Xu, Q.-H.; Lu, J.; Chhowalla, M.; Eda, G.; Loh, K. P. Molecularly Thin Two-Dimensional Hybrid Perovskites with Tunable Optoelectronic Properties Due to Reversible Surface Relaxation. *Nat. Mater.* **2018**, *17*, 908–914.
- (32) Cao, D. H.; Stoumpos, C. C.; Farha, O. K.; Hupp, J. T.; Kanatzidis, M. G. 2D Homologous Perovskites as Light-Absorbing Materials for Solar Cell Applications. *J. Am. Chem. Soc.* **2015**, *137*, 7843–7850.
- (33) Soe, C. M. M.; Nagabhushana, G. P.; Shivaramaiah, R.; Tsai, H.; Nie, W.; Blancon, J.-C.; Melkonyan, F.; Cao, D. H.; Traoré, B.; Pedesseau, L.; Kepenekian, M.; Katan, C.; Even, J.; Marks, T. J.; Navrotsky, A.; Mohite, A. D.; Stoumpos, C. C.; Kanatzidis, M. G. Structural and Thermodynamic Limits of Layer Thickness in 2D Halide Perovskites. *Proc. Natl. Acad. Sci. U. S. A.* **2019**, *116*, 58–66.
- (34) Mao, L.; Kennard, R. M.; Traore, B.; Ke, W.; Katan, C.; Even, J.; Chabinyc, M. L.; Stoumpos, C. C.; Kanatzidis, M. G. Seven-Layered 2D Hybrid Lead Iodide Perovskites. *Chem.* **2019**, *5*, 2593–2604.
- (35) Soe, C. M. M.; Stoumpos, C. C.; Kepenekian, M.; Traoré, B.; Tsai, H.; Nie, W.; Wang, B.; Katan, C.; Seshadri, R.; Mohite, A. D.; Even, J.; Marks, T. J.; Kanatzidis, M. G. New Type of 2D Perovskites with Alternating Cations in the Interlayer Space, (C(NH₂)₃)-(CH₃NH₃)_nPb_nI_{3n+1}: Structure, Properties, and Photovoltaic Performance. *J. Am. Chem. Soc.* **2017**, *139*, 16297–16309.
- (36) Li, N.; Zhu, Z.; Chueh, C.-C.; Liu, H.; Peng, B.; Petrone, A.; Li, X.; Wang, L.; Jen, A. K.-Y. Mixed Cation FA_xPEA_{1-x}PbI₃ with Enhanced Phase and Ambient Stability toward High-Performance Perovskite Solar Cells. *Adv. Energy Mater.* **2017**, *7*, 1601307.
- (37) Quan, L. N.; Yuan, M.; Comin, R.; Voznyy, O.; Beauregard, E. M.; Hoogland, S.; Buin, A.; Kirmani, A. R.; Zhao, K.; Amassian, A.; Kim, D. H.; Sargent, E. H. Ligand-Stabilized Reduced-Dimensionality Perovskites. *J. Am. Chem. Soc.* **2016**, *138*, 2649–2655.
- (38) Giovanni, D.; Lim, J. W. M.; Yuan, Z.; Lim, S. S.; Righetto, M.; Qing, J.; Zhang, Q.; Dewi, H. A.; Gao, F.; Mhaisalkar, S. G.; Mathews, N.; Sum, T. C. Ultrafast Long-Range Spin-Funneling in Solution-Processed Ruddlesden—Popper Halide Perovskites. *Nat. Commun.* **2019**, *10*, 3456.
- (39) Yuan, M.; Quan, L. N.; Comin, R.; Walters, G.; Sabatini, R.; Voznyy, O.; Hoogland, S.; Zhao, Y.; Beauregard, E. M.; Kanjanaboos, P.; Lu, Z.; Kim, D. H.; Sargent, E. H. Perovskite Energy Funnels for Efficient Light-Emitting Diodes. *Nat. Nanotechnol.* **2016**, *11*, 872–877.
- (40) Shi, J.; Gao, Y.; Gao, X.; Zhang, Y.; Zhang, J.; Jing, X.; Shao, M. Fluorinated Low-Dimensional Ruddlesden—Popper Perovskite Solar Cells with over 17% Power Conversion Efficiency and Improved Stability. *Adv. Mater.* **2019**, *31*, 1901673.
- (41) Hautzinger, M. P.; Dai, J.; Ji, Y.; Fu, Y.; Chen, J.; Guzei, I. A.; Wright, J. C.; Li, Y.; Jin, S. Two-Dimensional Lead Halide Perovskites Templated by a Conjugated Asymmetric Diammonium. *Inorg. Chem.* **2017**, *56*, 14991–14998.
- (42) Cheng, P.; Xu, Z.; Li, J.; Liu, Y.; Fan, Y.; Yu, L.; Smilgies, D.-M.; Müller, C.; Zhao, K.; Liu, S. F. Highly Efficient Ruddlesden—Popper Halide Perovskite PA₂MA₄Pb₅I₁₆ Solar Cells. *ACS Energy Lett.* **2018**, 3, 1975–1982.
- (43) Spanopoulos, I.; Hadar, I.; Ke, W.; Tu, Q.; Chen, M.; Tsai, H.; He, Y.; Shekhawat, G.; Dravid, V. P.; Wasielewski, M. R.; Mohite, A. D.; Stoumpos, C. C.; Kanatzidis, M. G. Uniaxial Expansion of the 2D Ruddlesden—Popper Perovskite Family for Improved Environmental Stability. *J. Am. Chem. Soc.* **2019**, *141*, 5518—5534.
- (44) Mao, L.; Ke, W.; Pedesseau, L.; Wu, Y.; Katan, C.; Even, J.; Wasielewski, M. R.; Stoumpos, C. C.; Kanatzidis, M. G. Hybrid

- Dion-Jacobson 2D Lead Iodide Perovskites. J. Am. Chem. Soc. 2018, 140, 3775-3783.
- (45) Whitfield, P. S.; Herron, N.; Guise, W. E.; Page, K.; Cheng, Y. Q.; Milas, I.; Crawford, M. K. Structures, Phase Transitions and Tricritical Behavior of the Hybrid Perovskite Methyl Ammonium Lead Iodide. *Sci. Rep.* **2016**, *6*, 35685.
- (46) Fraccarollo, A.; Cantatore, V.; Boschetto, G.; Marchese, L.; Cossi, M. *Ab Initio* Modeling of 2D Layered Organohalide Lead Perovskites. *J. Chem. Phys.* **2016**, *144*, 164701.
- (47) Glasser, L. Systematic Thermodynamics of Layered Perovskites: Ruddlesden–Popper Phases. *Inorg. Chem.* **2017**, *56*, 8920–8925
- (48) Smirnova, N. N.; Tsvetkova, L. Y.; Bykova, T. A.; Ruchenin, V. A.; Marcus, Y. Thermodynamic Properties of Tetrabutylammonium Iodide and Tetrabutylammonium Tetraphenylborate. *Thermochim. Acta* **2009**, *483*, 15–20.
- (49) Müller, P.; Saùl, A.; Leroy, F. Simple Views on Surface Stress and Surface Energy Concepts. *Adv. Nat. Sci.: Nanosci. Nanotechnol.* **2014**, *5*, 013002.
- (50) Cammarata, R. C. Surface and Interface Stress Effects in Thin Films. *Prog. Surf. Sci.* **1994**, *46*, 1–38.
- (51) Ferreira, A. C.; Létoublon, A.; Paofai, S.; Raymond, S.; Ecolivet, C.; Rufflé, B.; Cordier, S.; Katan, C.; Saidaminov, M. I.; Zhumekenov, A. A.; Bakr, O. M.; Even, J.; Bourges, P. Elastic Softness of Hybrid Lead Halide Perovskites. *Phys. Rev. Lett.* **2018**, *121*, 085502.
- (52) Faghihnasiri, M.; Izadifard, M.; Ghazi, M. E. DFT Study of Mechanical Properties and Stability of Cubic Methylammonium Lead Halide Perovskites (CH₃NH₃PbX₃, X = I, Br, Cl). *J. Phys. Chem. C* **2017**, *121*, 27059–27070.
- (53) She, L.; Liu, M.; Zhong, D. Atomic Structures of CH₃NH₃PbI₃ (001) Surfaces. ACS Nano **2016**, 10, 1126–1131.
- (54) Walsh, A. Principles of Chemical Bonding and Band Gap Engineering in Hybrid Organic–Inorganic Halide Perovskites. *J. Phys. Chem. C* **2015**, *119*, 5755–5760.
- (55) Piskunov, S.; Kotomin, E. A.; Heifets, E.; Maier, J.; Eglitis, R. I.; Borstel, G. Hybrid DFT Calculations of the Atomic and Electronic Structure for ABO₃ Perovskite (001) Surfaces. *Surf. Sci.* **2005**, *575*, 75–88.
- (56) Fechner, M.; Ostanin, S.; Mertig, I. Effect of the Surface Polarization in Polar Perovskites Studied from First Principles. *Phys. Rev. B: Condens. Matter Mater. Phys.* **2008**, 77, 094112.
- (57) Wang, D.; Liu, J.; Zhang, J.; Raza, S.; Chen, X.; Jia, C.-L. Ewald Summation for Ferroelectric Perovksites with Charges and Dipoles. *Comput. Mater. Sci.* **2019**, *162*, 314–321.
- (58) Bertaut, E. F. The Equivalent Charge Concept and Its Application to the Electrostatic Energy of Charges and Multipoles. *J. Phys. (Paris)* 1978, 12, 1331–1348.
- (59) Sapori, D.; Kepenekian, M.; Pedesseau, L.; Katan, C.; Even, J. Quantum Confinement and Dielectric Profiles of Colloidal Nanoplatelets of Halide Inorganic and Hybrid Organic–Inorganic Perovskites. *Nanoscale* **2016**, *8*, 6369–6378.
- (60) Stoumpos, C. C.; Soe, C. M. M.; Tsai, H.; Nie, W.; Blancon, J.-C.; Cao, D. H.; Liu, F.; Traoré, B.; Katan, C.; Even, J.; Mohite, A. D.; Kanatzidis, M. G. High Members of the 2D Ruddlesden-Popper Halide Perovskites: Synthesis, Optical Properties, and Solar Cells of (CH₃(CH₂)₃NH₃)₂(CH₃NH₃)₄Pb₅I₁₆. Chem. **2017**, *2*, 427–440.
- (61) Shenoy, V. B.; Reddy, C. D.; Ramasubramaniam, A.; Zhang, Y. W. Edge-Stress-Induced Warping of Graphene Sheets and Nanoribbons. *Phys. Rev. Lett.* **2008**, *101*, 245501.
- (62) Zhu, C.; Niu, X.; Fu, Y.; Li, N.; Hu, C.; Chen, Y.; He, X.; Na, G.; Liu, P.; Zai, H.; Ge, Y.; Lu, Y.; Ke, X.; Bai, Y.; Yang, S.; Chen, P.; Li, Y.; Sui, M.; Zhang, L.; Zhou, H.; et al. Strain Engineering in Perovskite Solar Cells and Its Impacts on Carrier Dynamics. *Nat. Commun.* **2019**, *10*, 815.
- (63) King-Smith, R. D.; Vanderbilt, D. Theory of Polarization of Crystalline Solids. *Phys. Rev. B: Condens. Matter Mater. Phys.* **1993**, 47, 1651–1654.

- (64) Natan, A.; Kronik, L.; Shapira, Y. Computing Surface Dipoles and Potentials of Self-Assembled Monolayers from First Principles. *Appl. Surf. Sci.* **2006**, *252*, 7608–7613.
- (65) Weller, M. T.; Weber, O. J.; Frost, J. M.; Walsh, A. Cubic Perovskite Structure of Black Formamidinium Lead Iodide, α -[HC(NH₂)₂]PbI₃, at 298 K. *J. Phys. Chem. Lett.* **2015**, *6*, 3209–3212.
- (66) Kresse, G.; Furthmüller, J. Efficiency of *Ab-Initio* Total Energy Calculations for Metals and Semiconductors Using a Plane-Wave Basis Set. *Comput. Mater. Sci.* **1996**, *6*, 15–50.
- (67) Kresse, G.; Hafner, J. Ab Initio Molecular-Dynamics Simulation of the Liquid-Metal—Amorphous-Semiconductor Transition in Germanium. Phys. Rev. B: Condens. Matter Mater. Phys. 1994, 49, 14251—14269.
- (68) Blöchl, P. E. Projector Augmented-Wave Method. Phys. Rev. B: Condens. Matter Mater. Phys. 1994, 50, 17953–17979.
- (69) Perdew, J. P.; Burke, K.; Ernzerhof, M. Generalized Gradient Approximation Made Simple. *Phys. Rev. Lett.* **1996**, 77, 3865–3868.
- (70) Grimme, S.; Antony, J.; Ehrlich, S.; Krieg, H. A Consistent and Accurate *Ab Initio* Parametrization of Density Functional Dispersion Correction (DFT-D) for the 94 Elements H-Pu. *J. Chem. Phys.* **2010**, 132, 154104.
- (71) Grimme, S.; Ehrlich, S.; Goerigk, L. Effect of the Damping Function in Dispersion Corrected Density Functional Theory. *J. Comput. Chem.* **2011**, 32, 1456–1465.